Ferrihydrite nanoparticles interaction with model lipid membranes

Claudia G. Chilom[a,1], Bogdan Zorilă[b,1], Mihaela Bacalum[b,*], Maria Bălăşoiu[c,d,e],
Roman Yaroslavtsev[f,g], Sergey V. Stolyar[f,g], Sergey Tyutyunnicov[d]

[a] Department of Electricity, Solid State and Biophysics, Faculty of Physics, University of Bucharest, Măgurele, Romania
[b] Department of Life and Environmental Physics, "Horia Hulubei" National Institute of Physics and Nuclear Engineering, Măgurele, Romania
[c] Department of Nuclear Physics, "Horia Hulubei" National Institute of Physics and Nuclear Engineering, Măgurele, Romania
[d] Joint Institute for Nuclear Research, Dubna, Russia
[e] Moscow Institute of Physics and Technology, Dolgoprudniy, Russia
[f] Siberian Federal University, Krasnoyarsk, Russia
[g] Kirensky Institute of Physics, SB RAS, Krasnoyarsk, 660036, Russia

ABSTRACT

In recent years was observed an increased interest towards the use of metal nanoparticles for various biomedical applications, such as therapeutics, delivery systems or imaging. As biological membranes are the first structures with which the nanoparticles interact, it is necessary to understand better the mechanisms governing these interactions. In the present paper we aim to characterize the effect of three different ferrihydrite nanoparticles (simple or doped with cooper or cobalt) on the fluidity of model lipid membranes. First we evaluated the physicochemical properties of the nanoparticles: size and composition. Secondly, their effect on lipid membranes was also evaluated using Laurdan, TMA-DPH and DPH fluorescence. Our results can help better understand the mechanisms involved in nanoparticles and membrane interactions.

1. Introduction

Due to their physicochemical characteristics (size, shape, chemical composition, solubility, charge, and surface roughness), nanomaterials can interfere at the nanoscale level with biomolecules and cells, thus making them promising devices, with a variety of applications in biomedicine, such as: drug delivery systems, biopharmaceutics, biomarkers, tissue engineering, etc (Mostafa et al., 2015; Salata, 2004). Particularly, iron oxide and oxyhydroxide nanoparticles have been comprehensively exploited for human benefits in numerous fields, from environmental problems to medical ones (Armanetti et al., 2018; Chilom et al., 2017; Dobrovolskaia et al., 2008; Faraji et al., 2010; Rajendran et al., 2017; Stolyar et al., 2018a,2018b; Wilkinson, 2003). One member of this family, with increasing interest in recent years, is ferrihydrite, a Fe(III) oxyhydroxide which can be found both in soils, but also in living organism complexed with the iron storage protein ferritin (Bauminger et al., 1994). In addition to natural form, different chemical and biological routes can be employed to synthetize nanoparticles with properties well controlled (Lima et al., 2008; Michel et al., 2007; Stolyar et al., 2018a, 2018b; Stolyar et al., 2017). However,

the same physicochemical properties that make them valuable can also manifest harmful effects against the living organisms or the environment (Xu et al., 2010; Yang et al., 2010). Even if previous studies reported the internalization of the nanoparticles which could lead to an increased cell cytotoxicity (Soenen et al., 2010, 2011; Valdiglesias et al., 2015), the mechanisms underlying iron oxide nanoparticles toxicity it is still unclear (Kornberg et al., 2017). Development of new synthesis techniques and especially the functionalization of nanoparticles with different molecules has contributed to reducing their toxicity (Namvar et al., 2014; Tran et al., 2018), thus making the understanding of the nanoparticles interaction with the cells even more vital. Cell membranes are the first structures with which the nanoparticles interact (Zanella et al., 2017) and fully understanding their interaction mechanisms is crucial for improving nanoparticle biocompatibility. Depending on the nanoparticle physicochemical properties, they can interact differently with the cell membranes. Small nanoparticles (NPs) with diameter < 10 nm, are more likely to form membrane channels (Deserno, 2004), while larger NPs (with diameter > 10 nm), usually penetrate into cells through membrane wrapping and internalization (Contini et al., 2018). The fastest and

---

* Corresponding author at: Department of Life and Environmental Physics, Horia Hulubei National Institute for Physics and Nuclear Engineering, Reactorului 30, Măgurele, 077125, Romania.
E-mail address: bmihaela@nipne.ro (M. Bacalum).
[1] These authors contributed equally to this work.
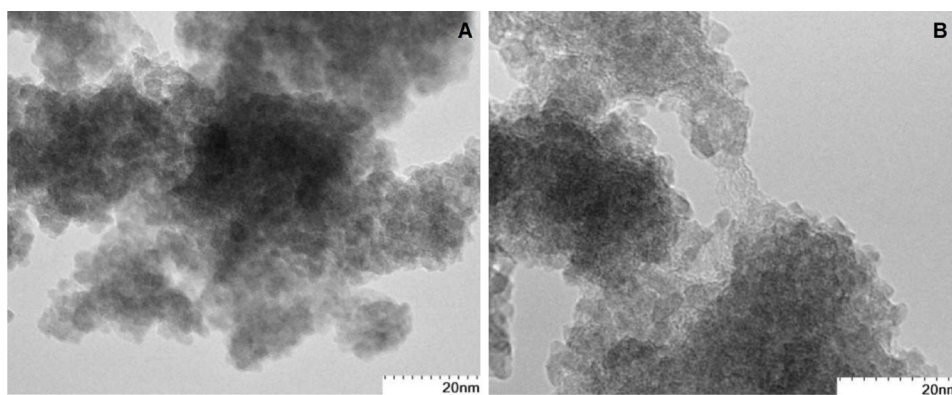
Fig. 1. TEM images of Co- Fh-NPs (A); Cu- Fh-NPs (B).

Table 1
The elemental composition of ferrihydrite nanoparticles.

Atomic elements	Fh-NPs		Co- Fh-NPs		Cu- Fh-NPs	
	[wt.%]	[at.%]	[wt.%]	[at.%]	[wt.%]	[at.%]
Fe	66.97	36.73	55.12	30.32	56.64	30.75
O	33.03	63.26	33.09	63.53	34.24	64.90
Me[a]	–	–	11.79	6.15	9.12	4.35

[a] Me – the metal used the dope the ferrihydrite nanoparticle.

easiest way to study the interaction of nanoparticles with lipid membranes is the use of liposomes as models of natural membranes (Li and Malmstadt, 2013; Zhang et al., 2012). Recent studies showed, that in the case of liposomes, the charged nanoparticles can induce membrane molecule movements (Petrov and Schutz, 2017), pattern formation and dynamic re-organization of liposome membrane (Chelladurai and Basu, 2018).

Up to now, only few studies addressed the effects of iron and other metal nanoparticles on the membrane fluidity (Mhashal and Roy, 2014; Santhosh et al., 2012, 2014). Hence, the aim of this study is to characterize the interaction of three ferrihydrite nanoparticles (Fh-NPs) with lipid membranes. Firstly, we characterized the nanoparticles by Transmition Electron Microscopy (TEM), Scanning electron microscopy-energy-dispersive X-ray analysis (SEM-EDX), Fourier transform infrared spectroscopy (FTIR), Atomic Force Microscopy (AFM) and Small-Angle Neutron Scattering (SANS). Secondly, we monitored the fluidity of lipid membranes using three fluorescent membrane probes: Laurdan, which is located at the level of the lipid head groups, 1-(4-Trimethylammoniumphenyl)-6-Phenyl-1,3,5-Hexatriene p-Toluene-sulfonate (TMA-DPH), which is located at the level of the glycerol backbone and upper segments of the phospholipid acyl chains (do Canto et al., 1858) and DPH which is distributed randomly in the hydrophobic core of the membrane (do Canto et al., 1858). The results are encouraging for future use of Fh-NPs in medical and nanotechnological applications.

2. Materials and methods

2.1. Materials

Laurdan, DPH and TMA-DPH were purchased from Invitrogen/Molecular Probes (Eugene, OR, USA). The lipids used, 1,2-dipalmitoyl-sn-glycero-3-phosphocholine (DPPC) and Cholesterol (Chol), were purchased from Avanti Polar Lipids (Alabaster, AL, USA). Na2HPO4·2H2O, KH2PO4 anhydrous, and NaCl were purchased from

Sigma-Aldrich and used to prepare the phosphate-buffered saline (PBS, 10 mM, pH 7.4).

2.2. Synthesis of ferrihydrite nanoparticles

Synthetic ferrihydrite particles were prepared at room temperature as previously described (Stolyar et al., 2017). Brefily, an alkaline NaOH solution (1 M) was added to a solution of ferric chloride FeCl$_3$ (0.02 M) with constant stirring until the pH reaches a neutral value. The Fh-NPs doped with cobalt or copper were prepared in a similar way, with the addition of cobalt or cooper salt solutions (CoSO$_4$, CuSO$_4$) under continuous stirring until a neutral pH is achieved. The ratio between the iron salt and the dopant metal salt was calculated so that in ferrihydrite the amount of dopant metal was 10 % relative to the total amount of metal (Fe + Co, Fe + Cu). The precipitates obtained were collected on filters, washed repeatedly and dried at room temperature. The final products were stored as dry powder at room temperature and freshly prepared before use. If not otherwise stated, for the experiments, the powders were dissolved in PBS at stock concentrations around 5 mM and before each use the samples were sonicated for 30 min in a water bath to assure dispersion of the nanoparticles.

2.3. The transmission electron microscopy (TEM)

The transmission electron microscopy (TEM) examination for coper-doped ferrihydrite nanoparticles was carried out on a Hitachi HT7700 transmission electron microscope (Collective User Center of the Krasnoyarsk Scientific Center) as described previously for undoped and Cobalt-doped ferrihydrite nanoparticles (Stolyar et al., 2017). For TEM analysis, the samples were prepared by suspending a small amount of powdered sample in distilled water, followed by dripping a drop of each liquid sample onto a slide.

2.4. Scanning electron microscopy-energy-dispersive X-ray analysis (SEM-EDX)

SEM-EDX recordings were performed for the copper-doped ferrihydrite using a Carl Zeiss EVO 60 scanning electron microscope as described previously (Stolyar et al., 2017). Ferrihydrite and cobalt-doped ferrihydrite were reported previously (Stolyar et al., 2017 and Stolyar et al., 2018a, 2018b).

2.5. Attenuated total reflectance-fourier transform infrared (ATR-FTIR)

NPs were characterized using a Tensor 27 spectrometer (Bruker), equipped with an ATR module. 5 μL of the aqueous stock solutions of
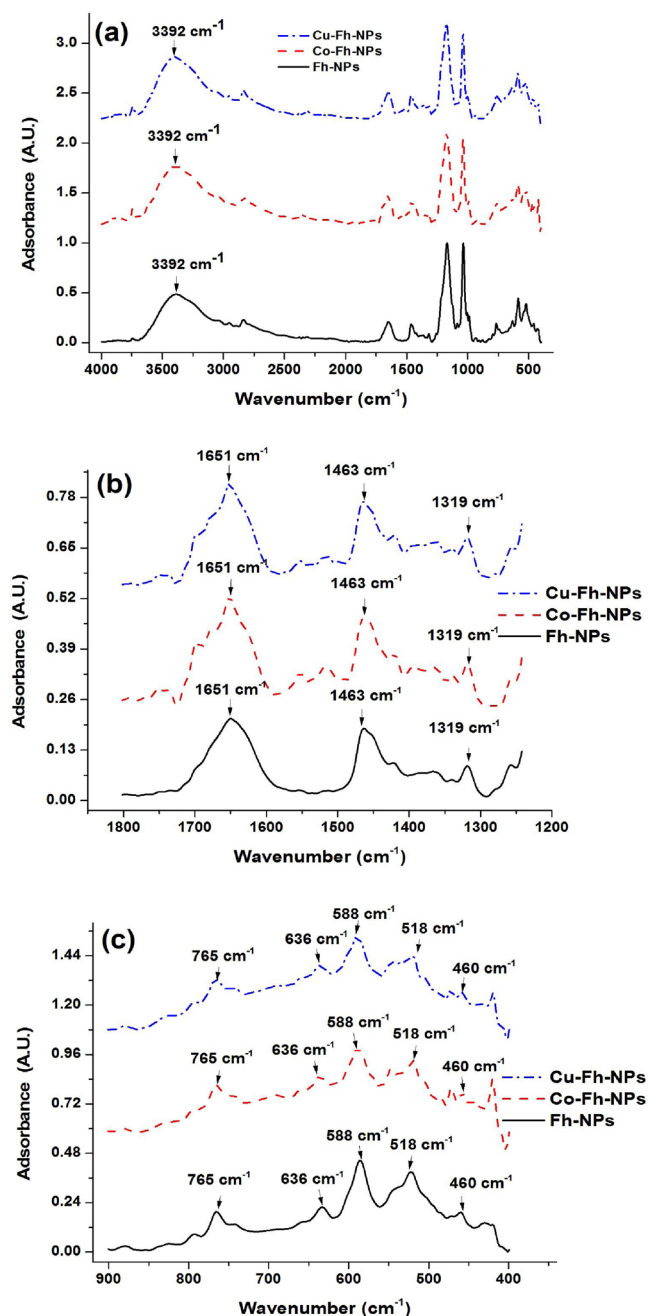
Fig. 2. ATR-FTIR spectra of Fh-NPs (black), Cu-Fh-NPs (blue) and Co-Fh-NPs (red) from rom 4000 to 400 cm^{-1}(a), 1800 to 1250 cm^{-1}(b), and 900 to 400 cm^{-1}(c).

nanoparticles was pipetted on the ATR crystal and let to dry before measurements. IR spectra were recorded between 400 and 4000 cm^{-1}, with a resolution of 4 cm^{-1} and 64 scans per sample. Spectra were further processed as described before (Chilom et al., 2018).

2.6. Atomic Force Microscopy (AFM)

Aqueous stock solutions of nanoparticles were diluted 10 times with bi-distilled water and a volume of 10 μL of the solution was pipetted on mica sheets. After deposition of nanoparticles on the mica sheets, they were dried for measurements in air. For AFM imaging, a NanoWizard 4

BioScience AFM (JPK instruments AG, Germany) was used. The images were recorded using the intermittent contact mode.

2.7. Small-Angle neutron scattering (SANS)

SANS measurements were performed on the time-of-flight YuMO spectrometer with two detector modes (Kuklin et al., 2018) in function at the IBR-2 high flux pulsed reactor (JINR Dubna). The SONIX + software system accomplished the control of the spectrometer (Kirilov et al., 2004). The experiments were carried out at a sample-to-detector distances of 4.5 m and 13 m, resulting in a scattering vector (Q) range of 0.006-0.6 Å-1. SANS experiments were accomplished on dried samples of ferihydrite, and Co- and Cu-dopped ferrihydrite.

2.8. Liposome preparation

Two types of large unilamelar vesicles (LUVs) with a final lipid concentration of 50 μM were prepared using the extrusion method according to the Avanti published protocol: (i) LUVs from DPPC and (ii) LUVs from DPPC:Chol (3:1) as described previously (Bacalum et al., 2013). Laurdan was added into the LUV suspension to a final lipid: probe ratio of 500:1. TMA-DPH and DPH were added to a final lipid:probe ratio of 100:1.

2.9. Steady state fluorescence

Steady-state fluorescence measurements were performed using a FluoroMax 3 spectrofluorimeter (Horiba Jobin Yvon, Edison, NJ, USA) equipped with a Peltier thermostatic cell holder. We used Laurdan, which incorporates into the membrane close to the polar head groups and can detect polarity changes in that region (Jay and Hamilton, 2017). Laurdan spectra were recorded in the range 400–600 nm, with the excitation set at 378 nm. The slits of excitation and emission monochromators were set at 3 nm. The recorded spectra were corrected for the spectral sensitivity of the emission channel of the spectrofluorimeter and for Raman and scattering artifacts. Two types of measurements were performed: (i) the effect induce by increasing concentration of NPs and (ii) the effect on the melting curve induced by incubation for 1 h or 24 h with the highest concentration of NPs. Laurdan fluorescence spectra and data processing were performed as described earlier (Bacalum et al., 2013; Zorilă et al., 2016). Generalized polarization (*GP*) was calculated as $(I_{440}-I_{490})/(I_{440}+I_{490})$, were I_{440} and I_{490} are the emission intensities at those wavelengths. We performed the same experiments using TMA-DPH, which is located in the upper region of the acyl chains (Kaiser and London, 1998; do Canto et al., 1858) and DPH which can be located in the hydrophobic core region of the membrane (do Canto et al., 1858). TMA-DPH and DPH anisotropy was recorded by exciting at 355 nm and recording the emission at 428 nm, with a 3 nm slit for both excitation and emission. All data were processed using the OriginPro 2016 software package (OriginLab Corporation, Northampton, MA, USA).

3. Results

3.1. Structural characterization of ferrihydrite samples by TEM

In order to directly analyze morphological and structural features of the ferrihydrite nanoparticles, TEM technique was used. Fh-NPs were previously characterized and are observed two diffuse reflections with interplanar distances d1 = 1.6 Å, d2 = 2.7 Å (Stolyar et al., 2017). In Fig. 1 are presented the images recorded for Co- Fh-NPs and Cu- Fh-NPs. All samples are in the nm order, but there are morphological differences between the nanoclusters of simple Fh-NPs (Stolyar et al.,
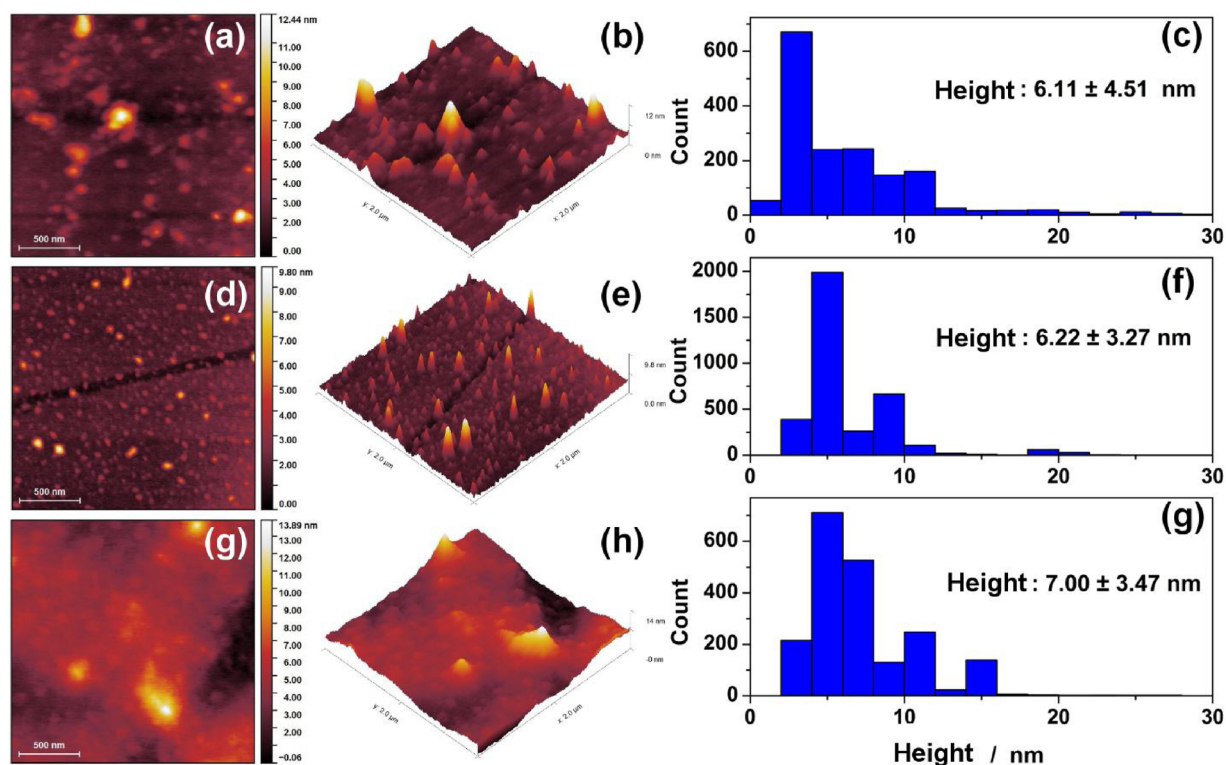
Fig. 3. Morphological characterization of Fh-NPs (a, b and c), Co-Fh-NPs (d, e and f) and Cu-NPs (g, h and i): topography (a, d, g), three dimensional (b, e, h) and histogram distribution of nanoparticles heights (c, f, i) images.
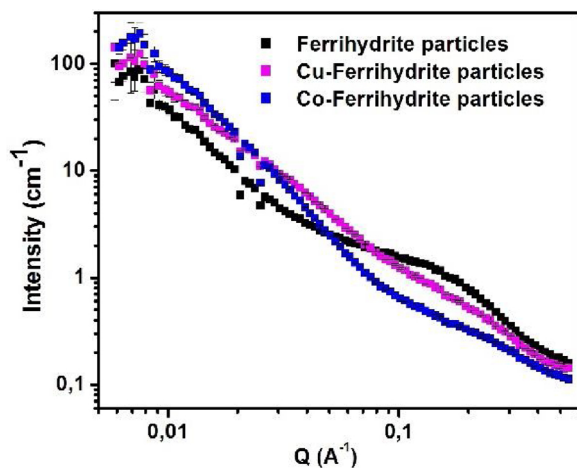
Fig. 4. SANS experimental data recorded for the ferrihydrite particles in the case of: synthetic simple Fh-NPs (black); synthetic Cu-Fh-NPs (magenta); synthetic Co-Fh-NPs (blue).

2017) and Co- Fh-NPs and Cu- Fh-NPs. The measured average particle size of ferrihydrite particles is ~2.5 nm (Stolyar et al., 2017). The doping with cobalt and coper leads to an increase of the particles to an average size of ~3.5 nm.

3.2. Elemental composition of ferrihydrite nanoparticles by SEM-EDX

SEM-EDX measurements allows us to characterize the elemental composition of the ferrihydrite nanoparticle. In Table 1 are reported the composition of Fh-NPs and Co- Fh-NPs (Stolyar et al., 2017) and also of

Cu- Fh-NPs. According to these results, the ratio of atomic concentrations of Fe/Co and Fe/Cu are 5/1 and respectively 7/1.

3.3. Ferrihydrite identification by ATR-FTIR spectroscopy

Ferrihydrite samples were first characterized by ATR-FTIR spectroscopy. In Fig. 2 can be observed the characteristic bands expected for these samples: (i) the O−H stretching signals, related to structural hydroxide, appear in a very broad band centered around 3380 cm^{-1} (Fig. 2a), (ii) the deformation mode of H_2O at ~1650 cm^{-1} (Fig. 2b), (iii) C−O stretching modes of adsorbed carbonate (1463 cm^{-1} for the asymmetric stretch and 1317 cm^{-1} for the symmetric stretch, Fig. 2b) and (iv) the Fe-O lattice stretching modes (Fig. 2c).

The stretching modes found for all three NPs were at 765, 588, 518, 460 and 420 cm^{-1}. However, for Cu and Co doped nanoparticles new bands were appeared between 460 and 518 cm^{-1}, but also around 410 cm^{-1}. Two new bands were also observed at 1514 and 1552 cm^{-1}, only for Cu and Co doped nanoparticles (Fig. 2b).

3.4. AFM morphological characterization of Ferrihydrite nanoparticles

Topological aspects and sizes of synthetic Fh-NPs were investigated by AFM. Fig. 3 displays AFM topological images of the three types of Fh-NPs. As observed, the nanoparticles display a roughly spherical shape. The average particle height for Fh-NPs is 6.11 ± 4.51 nm with nanoparticles varying between 2 nm and 30 nm. Co-Fh-NPs height is 6.22 ± 3.27 nm, with heights up to 20 nm. The Cu-Fh-NPs have a slightly larger height, of 7 ± 3.47 nm with a narrower distribution, between 3 and 16 nm.
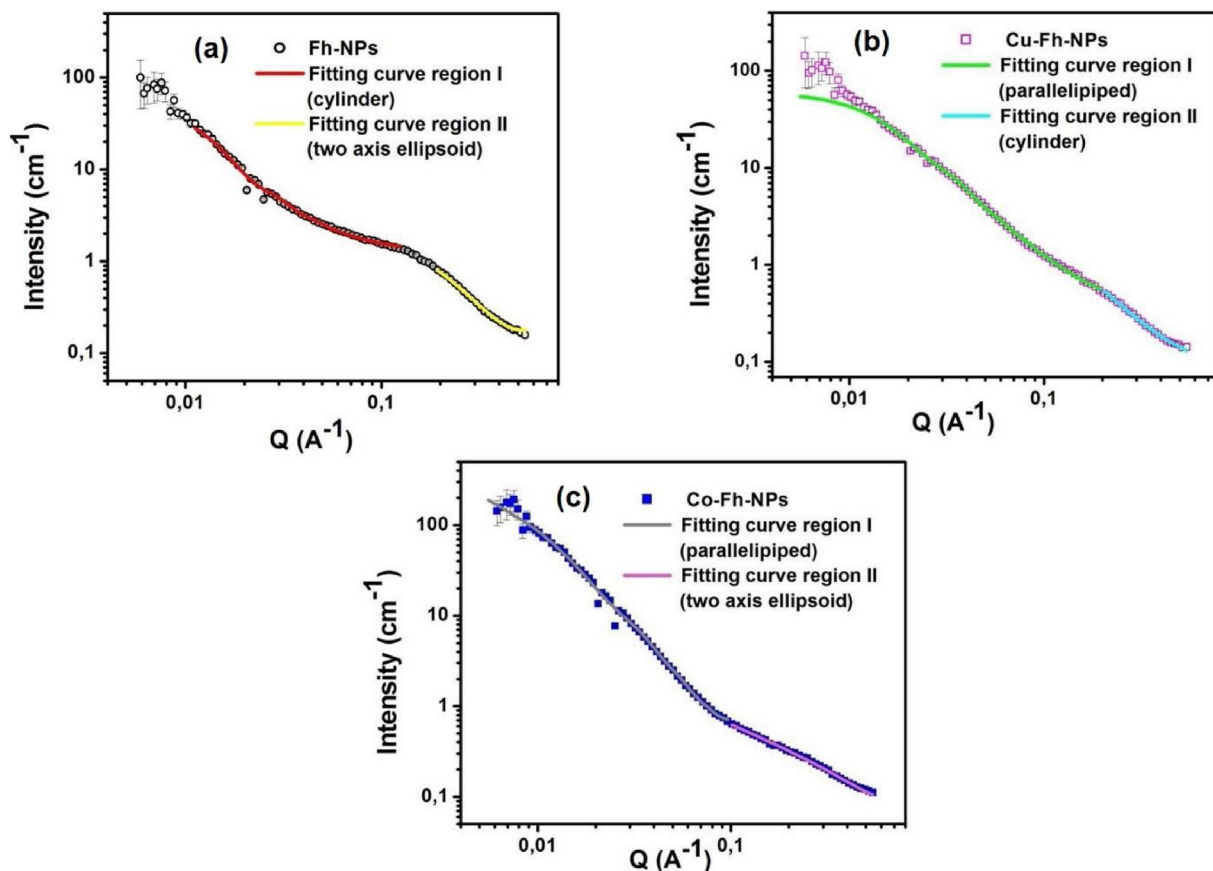
Fig. 5. The fitting curves of the experimental data for the scattering vector Q-range, 0.007 < Q < 0.05 Å-1 using the FITTER Program: (a) simple Fh-NPs; (b) Cu-Fh-NPs; (c) Co-Fh-NPs.

Table 2
The averaged dimensions for the Fh-NPs in the case of: synthetic particles (A); synthetic particles doped with Cu (B); synthetic particles doped with Co (C).

No.	Sample	Model	Dimensions [nm]
A	Ferrihydrite particles	Three axis ellipsoid	$a/2 = 4.51 \pm 0.21$ $b/2 = 54.92 \pm 8.26$ $c/2 = 34.41 \pm 4.08$
B	Cu - Ferrihydrite particles	Two axis core-shell ellipsoid	$(a/2)_{core} = 57.60 \pm 4.78$ $(b/2)_{core} = 7.08 \pm 0.19$ Shell thickness = 1.80 ± 0.59
C	Co - Ferrihydrite particles	Two axis core-shell ellipsoid	$(a/2)_{core} = 58.74 \pm 2.85$ $(b/2)_{core} = 6.73 \pm 0.52$ Shell thickness = 1.50 ± 0.17

3.5. Structure investigations of ferrihydrite samples by Small-Angle Neutron Scattering (SANS)

SANS was used to obtain information on the morphology and dimensions of simple and doped with Cu and Co ferrihydrite particles. SANS experimental curves (Fig. 4) were analyzed quantitatively by means of the FITTER Program (Soloviev et al., 2012).

The fitting curves of the experimental data for the scattering vector Q, 0.007 < Q < 0.05 Å-1 using a theoretical multi-parameter function through a set of data points for simple geometrical bodies are depicted in Fig. 5.

The fitting of the SANS experimental curves in the domain 0.007 < Q < 0.05 Å-1 (Fig. 5) gives the averaged dimensions for the investigated particles (Table 2). SANS results shows the particles are

agglomerated in 3D-clusters. The minimal dimensions of the clusters correspond to the particles radii and are in good agreement with those determined from AFM for each sample.

3.6. Effect of ferrihydrite nanoparticles on membrane fluidity

In order to check the nanoparticles effect on lipid membranes fluidity, we used two different liposomes (DPPC and DPPC:Chol) and performed the recordings using three membrane probes (Laurdan, TMA-DPH and DPH) as described in materials and methods.

In Fig. 6 are reported *GP* values (a and c) and the % *GP* changes (b and d) of NP-treated liposomes for both type of liposomes. A small increase in *GP* values can be observed with increasing concentrations of NPs.

The effects can be also observed in the graphs of % *GP* changes. Positive % *GP* changes indicate a rigidization of the membrane, while a negative % *GP* changes indicate a fluidization of the membrane. In the case of Fh-NPs, they almost don't affect the membrane of DPPC liposomes, while Cu-Fh-NPs and Co-Fh-NPs induce an increase of *GP* of 0.5 % and 1%, respectively. For DPPC:Chol LUVs, Fh-NPs and Cu-Fh-NPs don't affect the membrane, while Co-Fh-NPs slightly rigidize the membrane.

Following Laurdan measurements, we investigated the changes induce by increasing concentrations of NPs at the lipid hydrocarbon chains level with the help of TMA-DPH probe.

In Fig. 7 we show the anisotropy (a and c) and the % anisotropy changes of NP-treated liposomes from the control for both type of liposomes (b and d). Contrary to the results obtained from Laurdan
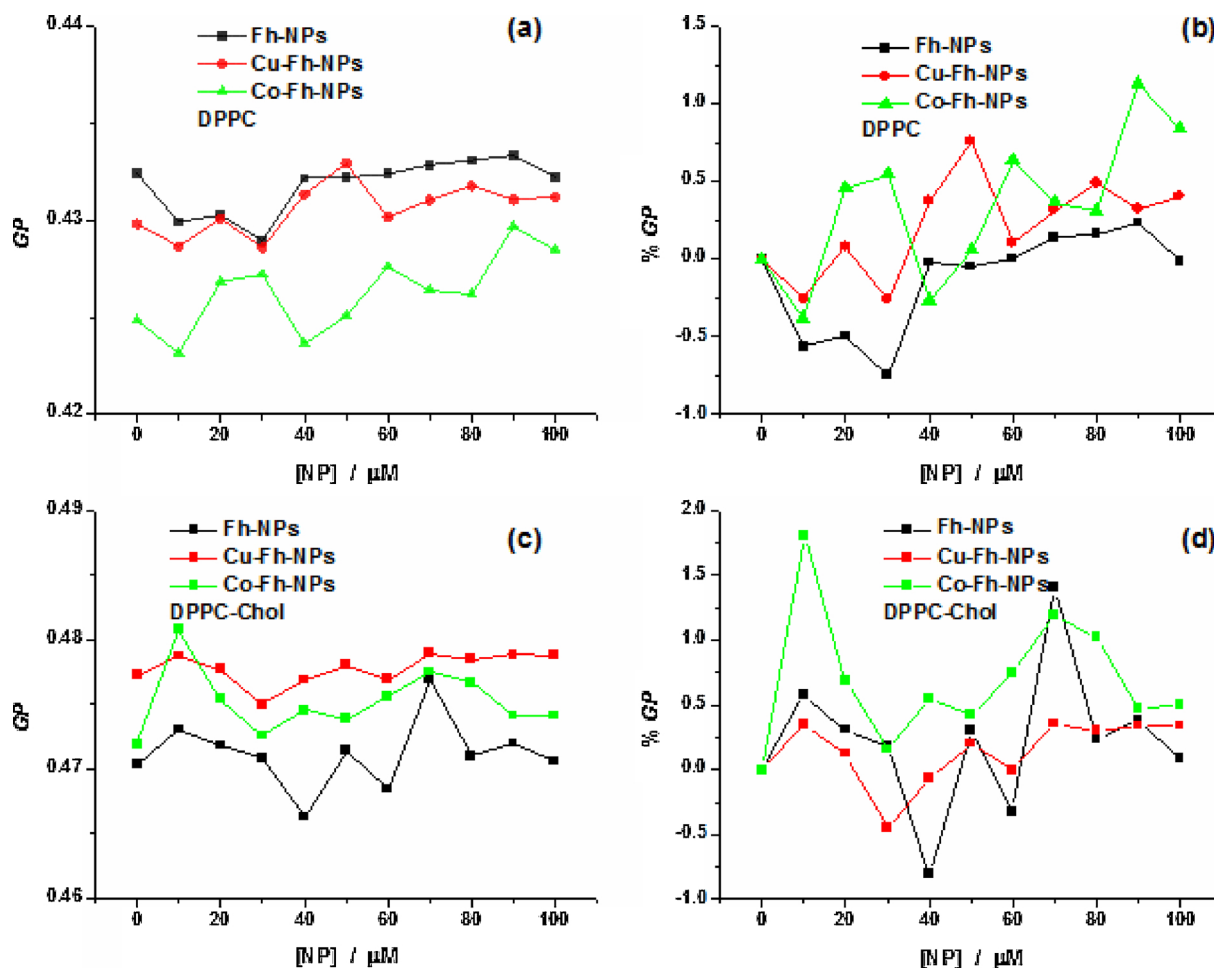
Fig. 6. (a and c) *GP* and (b and d) % *GP* of control liposomes compared to treated liposomes of various composition and concentrations of NPs. The plots are the averages of at least two independent experiments.

measurements, when TMA-DPH is used, for DPPC liposomes Fh-NPs induce an increase in anisotropy values, while Co and Cu-Fh-NPs induce a decrease in TMA-DPH anisotropy. For DPPC-Chol liposomes Fh-NPs and Co-Fh-NPs don't influence the membrane too much, while Cu-Fh-NPs induces a decrease in anisotropy.

The effects can be better highlighted in the graphs of % anisotropy changes (Fig. 7 b and d). In the case of Fh-NPs, they increase DPPC liposomes membrane rigidity by ∼ 0.5 %, while Cu-Fh-NPs and Co-Fh-NPs decrease membrane fluidity by 1.5 %, respectively. For DPPC:Chol, Fh-NPs and Co-Fh-NPs don't affect the membrane, while Cu-Fh-NPs decrease membrane fluidity up to 4%.

Finally, the DPH anisotropy was recorded for different concentrations of NPs and the results are reported in Fig. 8. When DPH is added to DPPC liposomes, the changes in anisotropy are smaller than observed for TMA-DPH, and are better observed in the % anisotropy graphs. Thus, we found that Fh-NPs and Co-Fh-NPs induce an increase in anisotropy values up to ∼ 0.5 % - 0.6 % (Fig. 8b), while Cu-Fh-NPs induce a decrease in DPH anisotropy with 0.6%. For DPPC-Chol liposomes Fh-NPs induce an increase in anisotropy up to 0.6%, while Co-Fh-NPs and Cu-Fh-NPs induces a decrease in anisotropy with 0.6 % (Fig. 8d).

Further on, we choose the highest concentration tested and recorded the melting curves of the liposomes after incubating them with NPs for 1 h and 24 h, respectively. In Fig. 9 are presented the melting curves of the two types of liposomes recorded from 20 to 60 °C in presence of 100 µM of NPs incubated for 1 h (a and c) and 24 h (b and

d), respectively. As can be seen, the *GP* values are decreasing with increasing temperatures for all experimental conditions. When checking the liposomes incubated for 1 h, we see that the nanoparticles did not affected the melting behavior of DPPC liposomes at temperatures below the transition temperature. However, at temperatures above the transition temperatures, the *GP* values are slightly increasing in the case of Cu-Fh-NPs. This indicates that the NPs interact more with the lipid heads at temperatures above the transition temperature, when the membrane is in a fluid phase. When the liposomes have Cholesterol, the Fh-NPs are not affecting the melting curves, while the Co and Cu-Fh-NPs are increasing the *GP* values at temperatures higher than 40 °C. These results indicate that the NPs are probably embedded on the membrane surface interacting with the head groups of lipids and thus leading to an increase in the order of the lipids.

In contrast, after 24 h of incubation, there is no significant change in the melting curves of the DPPC or DPPC:Chol liposomes.

The same experiments were repeated also using TMA-DPH (Fig. 10). As seen in Fig. 10, the nanoparticles did not affected the melting behavior of DPPC liposomes neither after 1 h or 24 h incubation. However, there are some changes observed in the case of DPPC;Chol liposomes. When the liposomes were incubated for 1 h, all NPs decreased the anisotropy, thus making the membrane more fluid, with the highest effect observed for Cu-Fh-NPs. However, after 24 h incubation, all NPs induced an increase in anisotropy, thus increasing the membrane rigidity with no difference between the effects induced by them. These
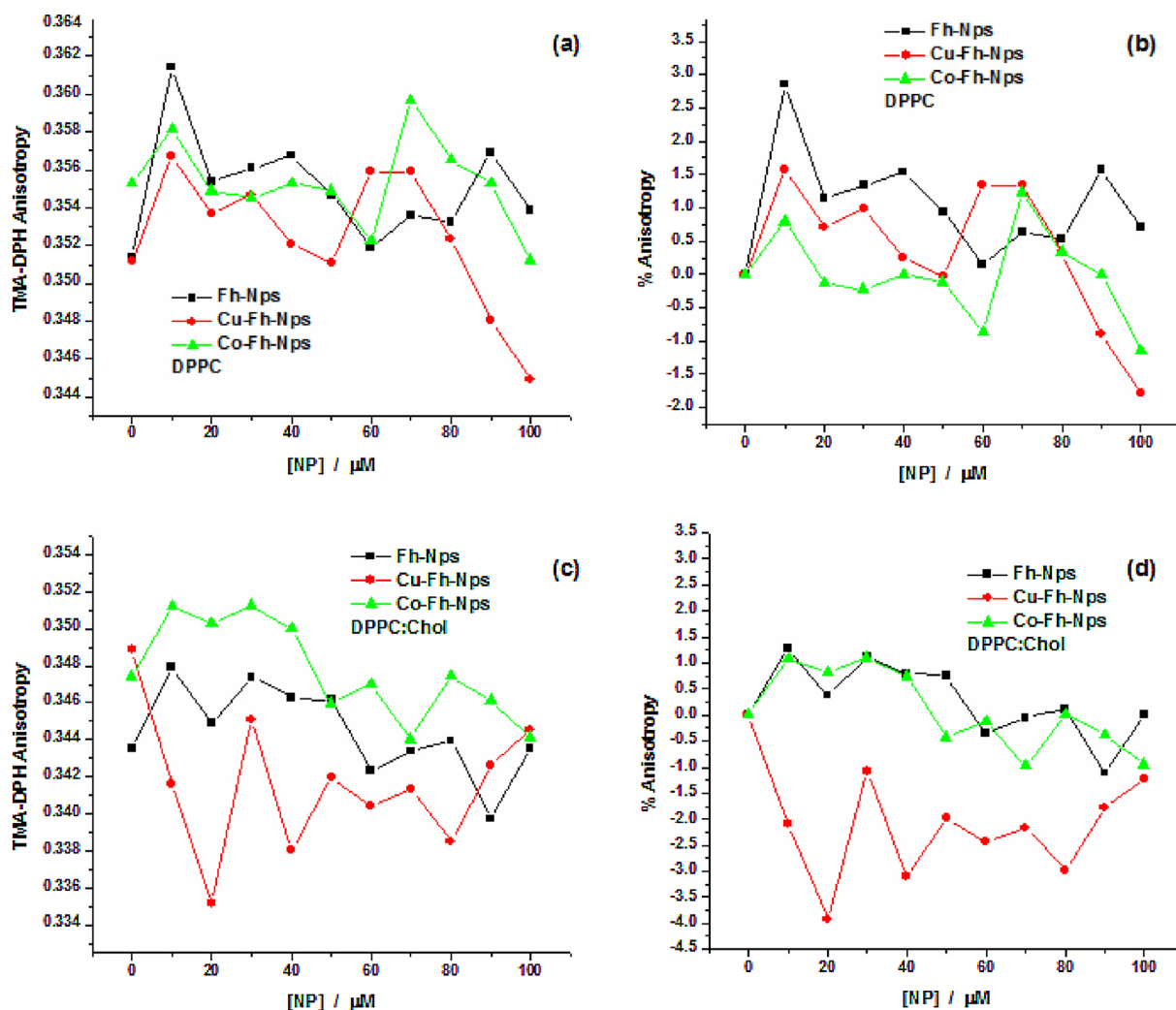
Fig. 7. (a and c) Anisotropy of TMA-DPH and (b and d) percent changes in anisotropy (% anisotropy) of control liposomes compared to treated liposomes of various composition and concentrations of NPs. The plots are the averages of at least two independent experiments.

results indicate that the NPs can get below the head groups of the lipids, thus affecting membrane fluidity, but only when there is also Cholesterol in the membrane.

The last experiments were performed using DPH (Fig. 11). Similar to TMA-DPH, the nanoparticles did not affected the melting behavior of DPPC liposomes neither after 1 h or 24 h incubation. However, there are some changes observed in the case of DPPC-Chol liposomes. When the liposomes were incubated for 1 h, both Co and Cu-Fh-NPs decreased the anisotropy, similar to what we observed in the case of TMA-DPH, thus making the membrane more fluid. A similar effect is still observed after 24 h incubation for all NPs. Contrary to TMA-DPH, DPH is distributed over the entire hydrophobic core of the membrane, thus sensing the changes induced at the level of lipid tails. Based on these results we can say that the NPs, when Cholesterol is present, can reach the hydrophobic core of the bilayer.

4. Discussions

Given the interest in the use of iron oxide and oxyhydroxide nanoparticles in medical applications, we have focused in this paper on the characterization of three types of Fh-NPs and their effects on the fluidity of artificial lipid membranes. Physicochemical properties of Fh-NPs can be modulated by doping them with transition metal cations, such as Co and Cu. Despite the increase cytotoxicity of the transition metals, the Fh-NPs can be doped with cation-controlled concentrations that do not compromise cellular biocompatibility. Thus, an initial structural characterization of these particles is necessary.

First, we showd using TEM that the morphology of the doped NPs is different from the one of Fh-NPs, with Fh-NPs having a size ~ 2.5 nm, while Co-Fh-NPs and Cu-Fh-NPs have a larger size, around 3.5 nm as seen in Fig. 1. Following this, we analyzed the ratio for atomic concentration for Cu- Fh-NPs and we found it to be 7/1 (Fe/Cu) (Table 1) as compared to 5/1 (Fe/Co) which was reported previously (Stolyar et al., 2017). Following this, we characterized the nanoparticles by ATR-FTIR measurements. Previous studies showed that the infrared spectrum of ferrihydrite is difficult to be interpreted, due to the degree of crystallinity/amorphicity, the extent of particle aggregation and the high reactivity with both gaseous and hydrous systems (Hausner et al., 2009). Also, depending on the methods used to prepare the samples the specific bands can fluctuate (Hausner et al., 2009). Even so, there are a few specific regions that can be assigned to ferrihydrite. One is the broad band characteristic for O−H stretching, which we found it at
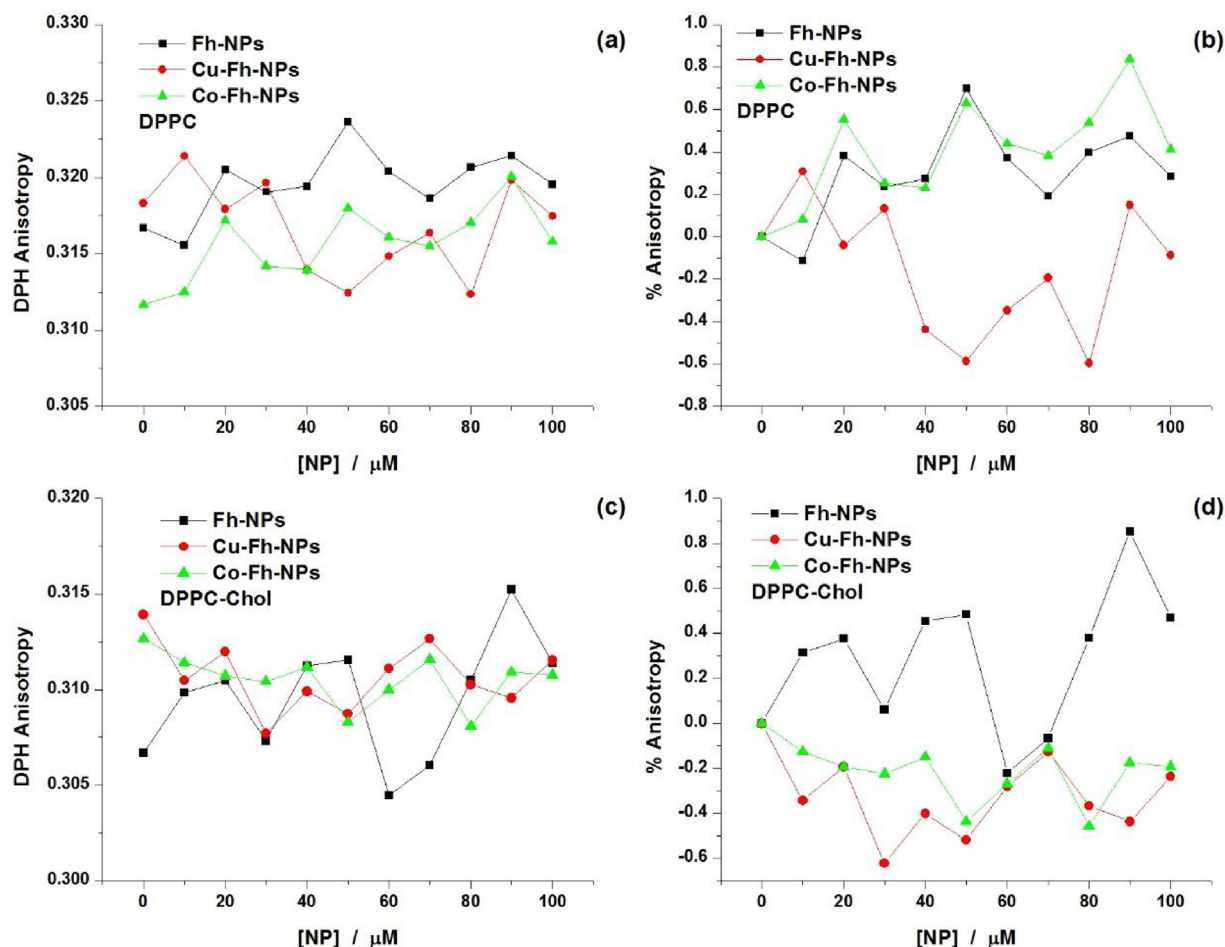
Fig. 8. (a and c) Anisotropy of DPH and (b and d) percent changes in anisotropy (% anisotropy) of control liposomes compared to treated liposomes of various composition and concentrations of NPs. The plots are the averages of at least two independent experiments.

$3380\,\mathrm{cm^{-1}}$ for all three samples (Fig. 2A). As described previously, the band shows the contribution of the structural hydroxide (Hausner et al., 2009). A second specific region (Hausner et al., 2009; Michel et al., 2007), was found between 1700 and $1200\,\mathrm{cm^{-1}}$, where we have three characteristic bands for Sorbed H_2O (around $1640\,\mathrm{cm^{-1}}$) and the C—O stretching modes (Fig. 2B). Similar water absorption band was found in Ca-Mg- doped Ferrihydrite NPs (Mohapatra et al., 2012) and α-Fe_2O_3 (Ristic et al., 2007). The last region specific for ferrihydrite is related to the Fe-O lattice and the values found are close to the ones reported previously in the literature (Mohapatra et al., 2012; Ristic et al., 2007). However, the differences observed between the bands found for our NPs and the ones reported previously are expected and can be attributed to a variety of factors, such as different preparation protocol, sample aggregation, the shape of the particles, etc (Anghel et al., 2012; Hausner et al., 2009; Kirilov et al., 2004; Michel et al., 2007; Villacis-Garcia et al., 2015). Finally, in case of Cu doped NPs, the absorption peak found around $470\,\mathrm{cm^{-1}}$ are due to Cu—O vibrations (Zhang et al., 2013). Similarly, for Co doped NPs, the absorption band found around $420\,\mathrm{cm^{-1}}$ is attributed to Co—O banding or stretching (Zahariev et al., 2017).

Following, the size of the nanoparticles was assessed using both AFM and SANS measurements. Both AFM images (Fig. 3) and scattering profile (Figs. 4 and 5) converge to similar results, showing that the Fh-NPs are generally spherical to ellipsoidal clusters, with heights varying

between $2-30$ nm. These values for all three types of Fh-NPs suggest a relatively amorphous structure of Fh-NPs that is consistent with results reported from TEM, but also the ones reported for the biogenic Fh-NPs from *Klebsiella oxytoca* (Chilom et al., 2017).

Considering that liposomes can be used as transport (Malam et al., 2009; Mujoo et al., 2018) or drug delivery systems for many compounds (Jain et al., 2013; Santhosh et al., 2015) it is important to first understand their effects on the lipid membrane, considering that the plasma membrane is the first barrier the NPs need to pass. The two main pathways of nanoparticles across the membrane are separated into endocytosis (phagocytosis, clathrin/caveolin dependent/independent or macropinocytosis) and direct penetration (diffusion, permeation and pore formation) (Qu et al., 2013). However, there are only a few numbers of experimental and theoretical studies that showed that different NPs properties can influence their uptake into cells (Behzadi et al., 2017; Foroozandeh and Aziz, 2018; Wang et al., 2008). The size and shape of the NPs are some of the most important ones and can decide the mechanism: endocytosis, penetration, diffusion, etc. Because the there is also the possibility to have more than one mechanism, we wanted first to focus on the passive mechanisms by studying the effects of the NPs on the lipid membrane of liposomes with different composition.

The effect of the NPs on membrane fluidity and the ordering parameter of the membrane was assessed using Laurdan, TMA-DPH and
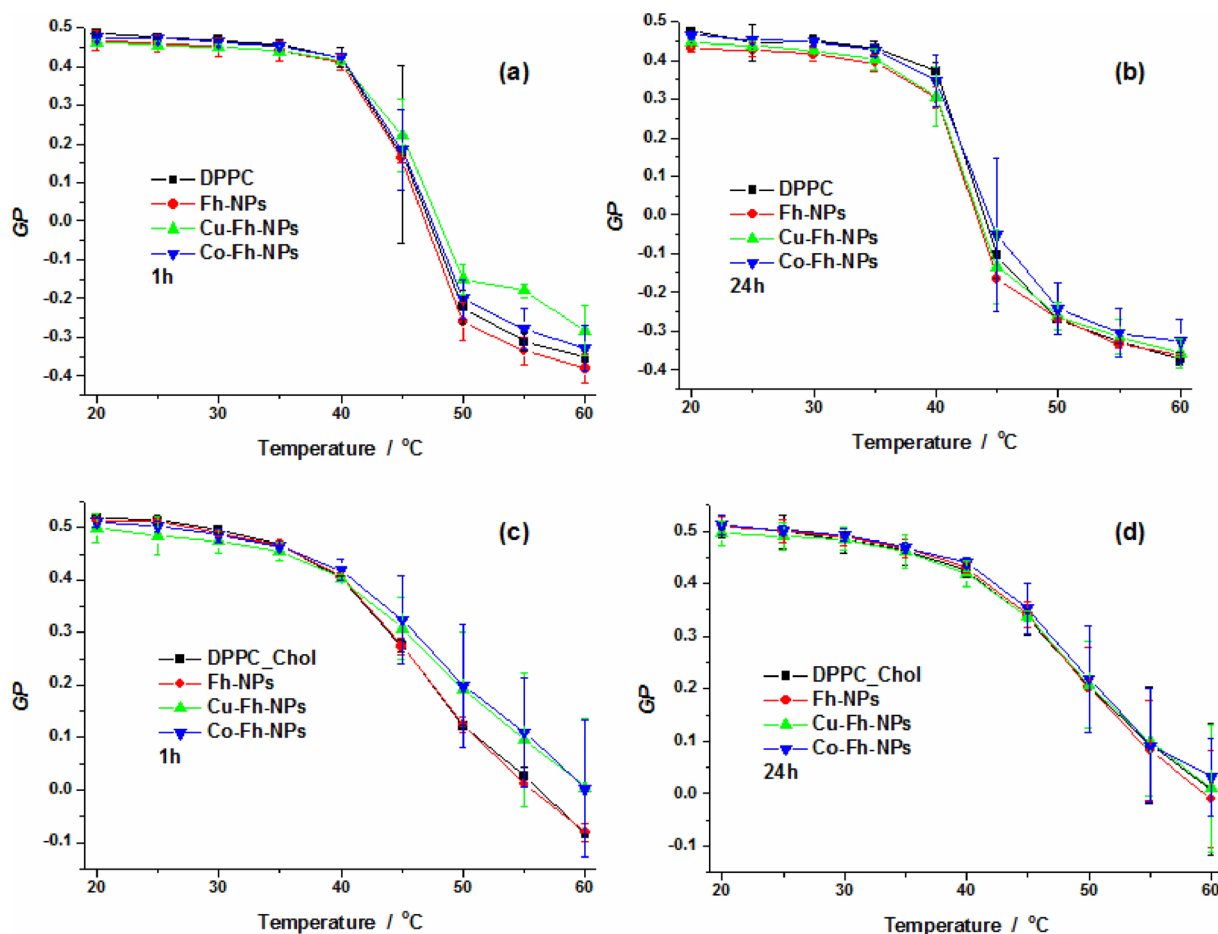
Fig. 9. Melting curves of DPPC (a and b) and DPPC:Chol (c and d) in presence or absence of nanoparticles at 1 h or 24 h incubation time.

DPH fluorescent probes. All three probe are wildly used to study membrane polarity and fluidity in both model and natural membranes (Bacalum et al., 2013; Bonaventura et al., 2014; Kuhry et al., 1983; Lentz, 1989, 1993). They are nonfluorescent in water, but they become fluorescent after incorporating in lipid membranes, where Laurdan probes the region below the lipid head groups (Stott et al., 2008), while TMA-DPH probes the glycerol backbone (Cundall et al., 1979), slightly lower than the region probed by Laurdan. Contrary, DPH will probe the entire region of the hydrophobic core of the membrane (do Canto et al., 1858).

Due to its localization inside the membrane, Laurdan changes in fluorescent spectra are correlated to changes in membrane polarity, more exactly reflecting the changes in the content of water molecules, thus an indirect measure of membrane fluidity (De Vequi-Suplicy et al., 2006; M'Baye et al., 2008). However, Laurdan detects changes caused both by variation in lipid composition, but also due the mobility of the lipid molecules surrounding it (Harris et al., 2002).

It is known that TMA-DPH and DPH fluorescence anisotropy values are comparable with lipid ordering parameter, thus a decrees of anisotropy values is correlated with increase in membrane fluidity (Wrobel et al., 2012; Santhosh et al., 2014).

Thus, after the structural features of the NPs were established, we further studied their effect on model lipid membranes. The studies reported until now in the literature, address this issue by using the anisotropy of the fluorescent probe diphenylhexatriene (DPH) or TMA-DPH (Bothun, 2008; Santhosh et al., 2015, 2012; Santhosh et al., 2014).

All the studies show that, if the NPs and the membranes are interacting, they can alter membrane fluidity.

We only found two studies reporting the use of the Laurdan as a fluorescent probe to monitor lipid packing (Bhat et al., 2016; Wei et al., 2017). In their study, Bhat and collaborators showed that the addition of gold nanoparticles with a diameter smaller than 30 nm increases the fluidity of DMPC liposomes (Bhat et al., 2016), while Wei and collaborators showed the importance of electrostatic forces formed between NPs and liposomes (Wei et al., 2017).

Considering that the nanoparticles size is on the range of membrane thickness, we expect that the nanoparticles can directly pass through the membrane, without any major interactions like wrapping around the nanoparticles or braking the lipid membranes.

When checking the effect of increasing concentration of NPs on the two types of liposomes we found that they will induce small changes in *GP* and anisotropy values, which indicates a small interaction of the NPs with the lipids. Following this, we were interested in understanding how the NPs affect the membrane fluidity after different incubation times. We recorded the transition temperature curves for DPPC LUVs, and we found, that independent of the incubation time, the NPs did not affect the membrane organization, neither at the head group region nor at the hydrocarbon tails for a gel phase membrane. This can be determined by the increased rigidity of the membrane and reduced mobility of the membrane components. However, when the membrane is in the fluid phase, in Laurdan loaded LUVs we observed a slight rigidization of the membrane when treated with NPs, indicating that the
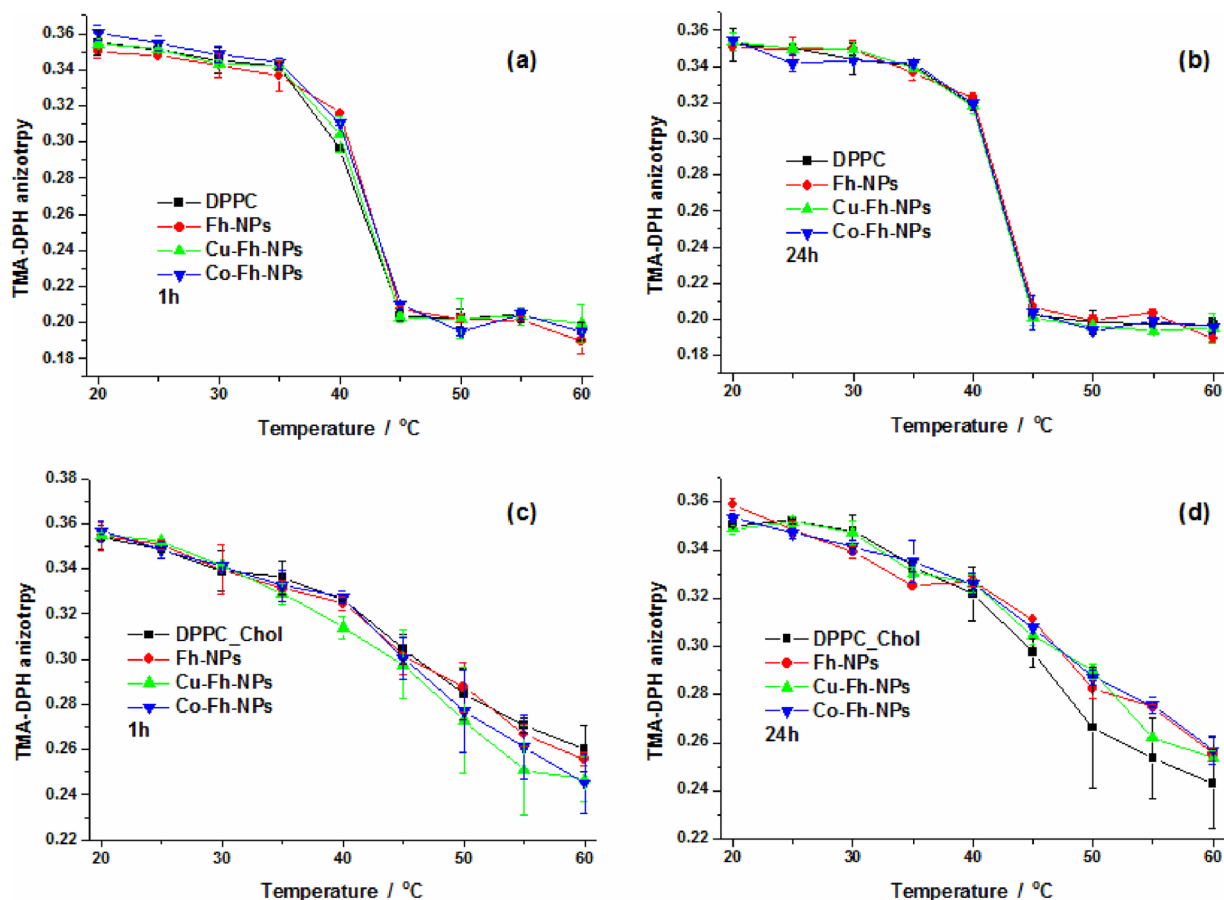
Fig. 10. TMA-DPH anisotropy temperature variation of DPPC (a and b) and DPPC:Chol (c and d) in presence or absence of NPs, at 1 h or 24 h incubation time.

NPs are interacting with the head groups of the lipids. The effect is lost when LUVs were incubated for 24 h with the NPs, indicating that the NPs are not interacting with the lipid head groups. When checking the anisotropy of TMA-DPH and DPH for DPPC LUVs, no significant changes are observed.

However, the presence of Cholesterol modulated the interactions between the liposomes and different types of NPs. The effects at the head groups' level are detected only for the shorter times of incubation and at temperatures higher than 40 °C. The presence of Co and Cu doped nanoparticle increases the *GP* values, thus making the region of the lipid head groups more packed, with less exposure of the Laurdan molecules to water. Contrary, the effects at the tails are observed for both incubation times. These results indicate that the NPs are able to also reach the interior of the bilayer, thus affecting membrane fluidity, as observed from the DPH anisotropy curves. This is expected considering that Cholesterol addition exerts considerable changes into the lipid membranes, by making the gel phase more fluid, while the fluid phase becomes more rigid (de Meyer and Smit, 2009). These causes an increase of the lipid order, thickness and stiffness of the membrane and depending on the lipid composition also to the segregation of lipid phases. These changes and also NPs characteristics (shape and size) can be responsible in the increase affinity of the NPs for the DPPC:Chol LUVs.

Similar results were also reported in (Santhosh et al., 2012, 2014). The results suggest that the NPs are interacting slightly with the lipid head groups for short exposer times (1 h), but, after a longer time, the NPs can be found predominantly in the hydrophobic core of the membrane and not embedded at the head group region. The results can

be justified also by the fact that the NPs were making pores in the membrane, or were entering in the vesicles by wrapping, the differences in GP and anisotropy values should have been larger.

The results are promising, however, further studies are needed to better characterize the effects at the level of biological or mimetic membranes, like: considering the charge of the lipids, a higher variety of lipids, presence of important membrane receptors, etc. However, because the effect appears to be modulated by cholesterol presence it can be an indicative that similar effects can be expected if the NPs are applied to biological membranes.

5. Conclusion

The results of this study showed that cholesterol presence in the membrane can modulate NPs effect on membrane organization. The NPs interact with the head of the lipids, for both type of vesicles for a short time, especially in when the membrane is in the fluid phase, while they change the environment around lipid chains only of DPPC:Chol LUVs, for all conditions tested. The results suggest that the NPs can localize at the level of the lipid tails when cholesterol is present in the membrane, however, further studies are needed to better characterize the effects in model membranes as well as biological membranes.

Declaration of Competing Interest

The authors declare no conflict of interest.
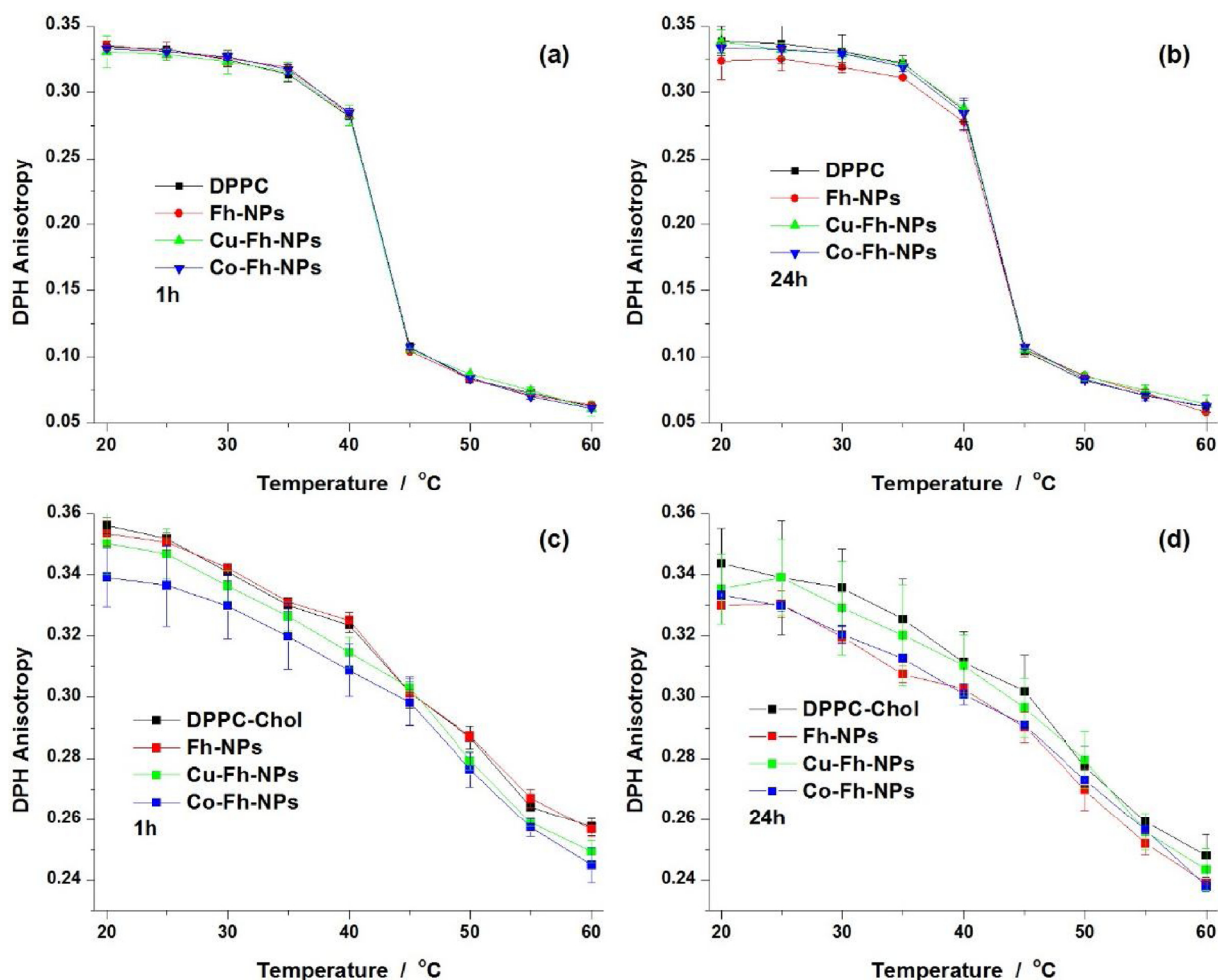
Fig. 11. DPH anisotropy temperature variation of DPPC (a and b) and DPPC:Chol (c and d) in presence or absence of NPs, at 1 h or 24 h incubation time.

Acknowledgements

References

Anghel, L., et al., 2012. Characterization of bio-synthesized nanoparticles produced by Klebsiella oxytoca. J. Phys. Conf. Ser. 351, 1–7.

Armanetti, P., et al., 2018. Spectroscopic and photoacoustic characterization of encapsulated iron oxide super-paramagnetic nanoparticles as a new multiplatform contrast agent. Spectrochim. Acta A. 199, 248–253.

Bacalum, M., et al., 2013. Fluorescence spectra decomposition by asymmetric functions: laurdan spectrum revisited. Anal. Biochem. 440 (2), 123–129.

Bauminger, E.R., et al., 1994. How does the ferritin core form? Hyperfine Interact. 91 (1), 835–839.

Behzadi, S., et al., 2017. Cellular uptake of nanoparticles: journey inside the cell. Chem. Soc. Rev. 46 (14), 4218–4244.

Bhat, A., et al., 2016. Effects of gold nanoparticles on lipid packing and membrane pore formation. Appl. Phys. Lett. 109 (26), 263106.

Bonaventura, G., et al., 2014. Laurdan monitors different lipids content in eukaryotic membrane during embryonic neural development. Cell Biochem. Biophys. 70 (2), 785–794.

Bothun, G.D., 2008. Hydrophobic silver nanoparticles trapped in lipid bilayers: size distribution, bilayer phase behavior, and optical properties. J. Nanobiotechnology 6, 1–10.

Chelladurai, R., Basu, J.K., 2018. Charged nanoparticle induced pattern formation and dynamic re-organisation on model biomembranes. J. Phys. D 51 (30), 1–9.

Chilom, C.G., et al., 2018. Insight into the interaction of human serum albumin with folic acid: a biophysical study. Spectrochim. Acta A. 204, 648–656.

Chilom, C.G., et al., 2017. Biomedical application of biogenic ferrihydrite nanoparticles. Rom. J. Phys. 62 (3-4), 1–13.

Contini, C., et al., 2018. Nanoparticle-membrane interactions. J. Exp. Nanosci. 13 (1), 62–81.

Cundall, R.B., et al., 1979. Photophysical properties of dph derivatives. Chem. Phys. Lett. 64 (1), 39–42.

de Meyer, F., Smit, B., 2009. Effect of cholesterol on the structure of a phospholipid bilayer. Proc Natl Acad Sci U S A. 106 (10), 3654–3658.

De Vequi-Suplicy, C.C., et al., 2006. Laurdan in fluid bilayers: position and structural sensitivity. J. Fluoresc. 16 (3), 431–439.

Deserno, M., 2004. Elastic deformation of a fluid membrane upon colloid binding. Phys. Rev. E 69 (3), 1–14.

Dobrovolskaia, M.A., et al., 2008. Method for analysis of nanoparticle hemolytic properties in vitro. Nano Lett. 8 (8), 2180–2187.

do Canto, A.M.T.M., et al., 1858. Diphenylhexatriene membrane probes DPH and TMA-DPH: a comparative molecular dynamics simulation study. Biochim. Biophys. Acta (11), 2647–2661.

Faraji, M., et al., 2010. Magnetic nanoparticles: synthesis, stabilization, functionalization, characterization, and applications. J. Iran Chem. Soc. 7 (1), 1–37.

Foroozandeh, P., Aziz, A.A., 2018. Insight into cellular uptake and intracellular trafficking of nanoparticles. Nanoscale Res. Lett. 13, 1–12.

Harris, F.M., et al., 2002. Use of laurdan fluorescence intensity and polarization to distinguish between changes in membrane fluidity and phospholipid order. BBABiomembranes 1565 (1), 123–128.

Hausner, D.B., et al., 2009. Ferrihydrite reactivity toward carbon dioxide. J. Colloid. Interf. Sci. 337 (2), 492–500.

Jain, A., et al., 2013. Dual drug delivery using "smart" liposomes for triggered release of anticancer agents. J. Nanopart. Res. 15 (7), 1–12.

Jay, A.G., Hamilton, J.A., 2017. Disorder amidst membrane order: standardizing laurdan generalized polarization and membrane fluidity terms. J. Fluoresc. 27 (1), 243–249.

Kaiser, R.D., London, E., 1998. Location of diphenylhexatriene (DPH) and its derivatives within membranes: comparison of different fluorescence quenching analyses of

membrane depth. Biochemistry. 37 (22), 8180–8190.

Kirilov, A.S., et al., 2004. Evolution of the SONIX software package for the YuMO spectrometer at the IBR-2 reactor. Instrum. Exp. Tech. 47 (3), 334–345.

Kornberg, T.G., et al., 2017. Potential toxicity and underlying mechanisms associated with pulmonary exposure to Iron oxide nanoparticles: conflicting literature and unclear risk. Nanomaterials 7 (10), 1–26.

Kuhry, J.G., et al., 1983. Tma-dph - a suitable fluorescence polarization probe for specific plasma-membrane fluidity studies in intact living cells. Cell Biophys. 5 (2), 129–140.

Kuklin, A.I., et al., 2018. High-throughput SANS experiment on two-detector system of YuMO spectrometer. J. Phys. Conf. Ser. 994, 1–7.

Lentz, B.R., 1989. Membrane fluidity as detected by diphenylhexatriene probes. Chem. Phys. Lipids 50 (3-4), 171–190.

Lentz, B.R., 1993. Use of fluorescent-probes to monitor molecular order and motions within liposome bilayers. Chem. Phys. Lipids 64 (1-3), 99–116.

Li, S., Malmstadt, N., 2013. Deformation and poration of lipid bilayer membranes by cationic nanoparticles. Soft Matter 9 (20), 4969–4976.

Lima, E., et al., 2008. Magnetic characterization of ferrihydrite nanoparticles synthesized by hydrolysis of Fe metal-organic precursor. Physica B 403 (23-24), 4156–4159.

M'Baye, G., et al., 2008. Liquid ordered and gel phases of lipid bilayers: fluorescent probes reveal close fluidity but different hydration. Biophys. J. 95 (3), 1217–1225.

Malam, Y., et al., 2009. Liposomes and nanoparticles: nanosized vehicles for drug delivery in cancer. Trends Pharmacol. Sci. 30 (11), 592–599.

Mhashal, A.R., Roy, S., 2014. Effect of gold nanoparticle on structure and fluidity of lipid membrane. PLoS One 9 (12), 1–18.

Michel, F.M., et al., 2007. The structure of ferrihydrite, a nanocrystalline material. Science 316 (5832), 1726–1729.

Mohapatra, M., et al., 2012. Ca-Mg-Doped surface-modified nano-sized ferrihydrite powder synthesized by surfactant mediation-precipitation technique: a novel super adsorbent for cations. Adsorp. Sci. Technol. 30 (5), 383–397.

Mostafa, A.A., et al., 2015. Evaluation of biological activities of chemically synthesized silver nanoparticles. J. Nanomater. 789178, 1–7.

Mujoo, H., et al., 2018. A real-time in vitro assay to evaluate the release of macro-molecules from liposomes. Drug Test. Anal. 10 (6), 1025–1032.

Namvar, F., et al., 2014. Cytotoxic effect of magnetic iron oxide nanoparticles synthesized via seaweed aqueous extract. Int. J. Nanomed. Nanosurg. 9, 2479–2488.

Petrov, E.P., Schutz, G.J., 2017. Molecular movements in biomembranes. J. Phys. D 50 (6), 1–3.

Rajendran, K., et al., 2017. Evaluation of cytotoxicity of hematite nanoparticles in bacteria and human cell lines. Colloids Surf. B Biointerfaces 157, 101–109.

Ristic, M., et al., 2007. Transformation of low crystalline ferrihydrite to alpha-Fe2O3 in the solid state. J. Mol. Struct. 834, 454–460.

Qu, Z.G., et al., 2013. Advances in the understanding of nanomaterial-biomembrane interactions and their mathematical and numerical modeling. Nanomedicine 8 (6), 995–1011.

Salata, O., 2004. Applications of nanoparticles in biology and medicine. J. Nanobiotechnology 2 (1), 1–6.

Santhosh, P.B., et al., 2015. Effect of superparamagnetic iron oxide nanoparticles on fluidity and phase transition of phosphatidylcholine liposomal membranes. Int. J. Nanomed. Nanosurg. 10, 6089–6104.

Santhosh, P.B., et al., 2012. A study on the interaction of nanoparticles with lipid membranes and their influence on membrane fluidity. J. Phys. Conf. Ser. 398, 1–6.

Santhosh, P.B., et al., 2014. Influence of nanoparticle-membrane electrostatic interactions on membrane fluidity and bending elasticity. Chem. Phys. Lipids 178, 52–62.

Soenen, S.J., et al., 2010. High intracellular iron oxide nanoparticle concentrations affect cellular cytoskeleton and focal adhesion kinase-mediated signaling. Small 6 (7), 832–842.

Soenen, S.J.H., et al., 2011. Cytotoxic effects of iron oxide nanoparticles and implications for safety in cell labelling. Biomaterials 32 (1), 195–205.

Soloviev, A.G., et al., 2012. FITTER. The package for fitting a chosen theoretical multi-parameter function through a set of data points. Application to experimental data of the YuMO spectrometer. J. Phys. Conf. Ser. 351, 1–15.

Stolyar, S.V., et al., 2018a. Bacterial ferrihydrite nanoparticles: preparation, magnetic properties, and application in medicine. J. Supercond. Nov. Magn. 31 (8), 2297–2304.

Stolyar, S.V., et al., 2017. Magnetic and resonance properties of ferrihydrite nanoparticles doped with cobalt. Phys. Solid State 59 (3), 555–563.

Stolyar, S.V., et al., 2018b. Preparation, structure and magnetic properties of synthetic ferrihydrite nanoparticles. J. Phys. Conf. Ser. 994, 012003.

Stott, B.M., et al., 2008. Use of fluorescence to determine the effects of cholesterol on lipid behavior in sphingomyelin liposomes and erythrocyte membranes. J. Lipid Res. 49 (6), 1202–1215.

Tran, P.A., et al., 2018. In vitro cytotoxicity of iron oxide nanoparticles: effects of chitosan and polyvinyl alcohol as stabilizing agents. Mater. Res. Express 5 (3), 1–7.

Valdiglesias, V., et al., 2015. Effects of iron oxide nanoparticles: cytotoxicity, genotoxicity, developmental toxicity, and neurotoxicity. Environ. Mol. Mutagen. 56 (2), 125–148.

Villacis-Garcia, M., et al., 2015. Laboratory synthesis of goethite and ferrihydrite of controlled particle sizes. B. Soc. Geol. Mex. 67 (3), 433–446.

Wang, B., et al., 2008. Nanoparticle-induced surface reconstruction of phospholipid membranes. PNAS 105 (47), 18171–18175.

Wei, X., et al., 2017. Effect of oxide nanoparticles on the morphology and fluidity of phospholipid membranes and the role of hydrogen bonds. J. Environ. Sci. China (China) 57, 221–230.

Wilkinson, J.M., 2003. Nanotechnology applications in medicine. Med. Device Technol. 14 (5), 29–31.

Wrobel, D., et al., 2012. Cationic carbosilane dendrimers-lipid membrane interactions. Chem. Phys. Lipids 165 (4), 401–407.

Xu, M.S., et al., 2010. Contribution of physicochemical characteristics of nano-oxides to cytotoxicity. Biomaterials 31 (31), 8022–8031.

Yang, Z., et al., 2010. A review of nanoparticle functionality and toxicity on the central nervous system. J. Royal Soc. Interface 7, S411–S422.

Zahariev, I., et al., 2017. FTIR Spectroscopy Method for Investigation of the Co-Ni Nanoparticle Nanosurface Phenomena. J. Chem. Technol. Metall. 52 (5), 916–928.

Zanella, D., et al., 2017. Iron oxide nanoparticles can cross plasma membranes. Sci. Rep. 7, 1–10.

Zhang, S., et al., 2012. Freezing or wrapping: the role of particle size in the mechanism of nanoparticle-biomembrane interaction. Langmuir 28 (35), 12831–12837.

Zhang, Y.X., et al., 2013. Controlled synthesis of hierarchical CuO nanostructures for electrochemical capacitor electrodes. Int. J. Electrochem. Sc. 8 (6), 8645–8661.

Zorilă, B., et al., 2016. Log-normal deconvolution of Laurdan fluorescence spectra - a tool to assess lipid membrane fluidity. Rom. Rep. Phys. 68 (2), 702–712.